AIAA JOURNAL
Vol. 48, No. 2, February 2010

# Scalar Spatial Correlations in a Supersonic Mixing Flowfield

Hidemi Takahashi,* Hiroki Oso,† Toshinori Kouchi,‡ and Goro Masuya§
*Tohoku University, Sendai 980-8579, Japan*
and
Mitsutomo Hirota¶
*Muroran Institute of Technology, Muroran 050-8585, Japan*

DOI: 10.2514/1.44684

**Single-time two-point spatial correlations of injectant concentrations in the supersonic mixing flowfield produced by a sonic transverse injection of air into a Mach 2.0 supersonic airstream were investigated using acetone planar laser-induced fluorescence data. Side-view and end-view contour maps were obtained in several planes to characterize the turbulent structure and three-dimensionality of the mixing flowfield. The correlation maps indicated an organized large-scale structure in the upper region of the jet. The side-view correlation maps revealed that the shape of the large dominating structure was elliptic and that its major axis turned from backward-leaning to forward-leaning as the reference point of correlation moved downstream. The end-view correlation maps showed that the instantaneous jet plume appeared by turns either in the top or in the lower sides of the time-averaged injectant plume in each cross section.**

## Nomenclature

$A$ = area of correlated region, m$^2$
$C$ = molar concentration, mol/m$^3$
$D$ = diameter of injection port, m
$D_{\mathrm{eq}}$ = equivalent diameter, m
$J$ = jet-to-freestream momentum flux ratio
$M$ = Mach number
$Mc$ = local convective Mach number
$m$ = molecular weight, kg/mol
$N$ = total number of samples
$P$ = local static pressure, Pa
$r$ = spatial correlation coefficient
$S$ = fluorescence signal intensity
$T$ = local static temperature, K
$U$ = streamwise velocity, m/s
$x$ = streamwise coordinate, m
$y$ = transverse coordinate, m
$z$ = spanwise coordinate, m
$\alpha$ = inclination angle of the large-scale structure to the horizontal axis, deg
$\gamma$ = specific heat ratio
$\lambda_B$ = Batchelor scale
$\rho$ = density, kg/m$^3$
$\chi$ = mole fraction

*Subscripts*

acetone = component of acetone
exit = flow condition at jet exit
$i$ = index number of samples
$j$ = jet
$m$ = main flow
mixture = acetone–air mixture gas
obj = object location against the reference location
1/2 = half-value of the local maxima

## I. Introduction

DETAILED understanding of the fuel–air mixing mechanism in a supersonic flowfield is vital to the successful design of hypersonic propulsive devices such as a scramjet engine. In this engine, fuel mixes with air flowing in the combustor at supersonic speed. Enhancement of fuel–air mixing is of great concern, since fuel injected into the supersonic airstream is not likely to mix quickly, because the two-dimensional vortex structure, which plays an important role in the mixing of low-speed turbulent flows, may be inhibited due to the compressibility effect. Low shear between fuel and air flow is another possible reason for poor mixing. This kind of flowfield is highly complex, three-dimensional, and turbulent; hence, it is difficult to investigate and characterize the mechanism of fuel–air mixing.

The recent development of highly resolved techniques in optical measurement enabled us to examine the structure of the flowfields produced by a normal sonic jet injected into a supersonic crossflow [1,2]. Takahashi et al. [1] examined the availability and benefits of using acetone planar laser-induced fluorescence (PLIF) in the supersonic mixing flowfield. VanLerberghe et al. [2] examined the same flowfield, but they mainly investigated the instantaneous mixing characteristics that are especially produced by the large-scale structures. They studied the flowfield with instantaneous, mean, and standard deviation images and image-intensity probability density functions. Both results revealed that instantaneous fuel distributions were very different from time-averaged ones, thus confirming the importance of investigation based on instantaneous data. The existence of the large-scale structure, which is similar to the well-recognized structure [3] in a low-speed flow, was observed even in such compressible flowfields, and this structure dominated the mixing mechanism. However, because of difficulty with directly resolved measurement, more detailed characteristics of the large-scale structure, such as behaviors and shapes of the structure, in the supersonic mixing flowfield are not yet fully understood.

To clarify details of the large-scale structure, investigation based on statistical treatment of instantaneous fluctuating data (e.g., correlation analysis) is quite meaningful. Single-time two-point spatial correlations taken from multiple images give the shape and spatial

---

Presented as Paper 23 at the 47th AIAA Aerospace Sciences Meeting, Orlando, FL, 5–8 January 2009; received 1 April 2009; revision received 30 July 2009; accepted for publication 19 August 2009.

*Japan Society for the Promotion of Science Research Fellow, Department of Aerospace Engineering; currently Postdoctoral Fellow, Department of Mechanical and Aerospace Engineering, University of Florida. Member AIAA.

†Graduate Student, Department of Aerospace Engineering.

‡Assistant Professor, Department of Aerospace Engineering. Member AIAA.

§Professor, Department of Aerospace Engineering, Senior Member AIAA.

¶Lecturer, Department of Mechanical Systems Engineering.

extent of a large-scale turbulent structure and resulting mixing mechanisms. They also indicate the influence of the surrounding flowfield (such as velocity distribution, shock waves, and boundary layers) on the structure.

Previous studies applied correlation analyses mainly to the velocity fields to investigate turbulent statistics (e.g., turbulent intensity in the boundary layer [4] in the axisymmetric jet [5] and in the boundary layer on the riblet surface [6]) as well as to find vortex structures (e.g., hairpin vortices in the channel flow [7] and in the supersonic turbulent boundary layer [8]). Correlations of the fluctuating scalar fields have also been conducted by employing several flow visualization techniques to investigate the spatial organizations and characteristics of the large-scale structure in the supersonic flowfield. Messersmith and Dutton [9] and Smith and Dutton [10] used planar Mie scattering from condensed ethanol droplets to examine the structure within the supersonic shear layers. They found that the structures were elongated and compressed toward the streamline flow direction with increasing compressibility. They also quantified an increase in size and a reduction in the eccentricity of the large-scale structure with increasing compressibility. Miles and Lempert [11] used UV Rayleigh scattering to obtain density fluctuations and investigated the shock-wave/boundary-layer interactions. They found an orientation in the structure and determined that the size of the structure was significantly influenced by the extent of compressibility. The objectives of these studies were mostly to investigate the mixing layer between two parallel flows. For the transverse injection flowfield similar to the one studied in the present work, Gruber et al. [12] investigated the compressibility effect by examining the convective Mach number for injection of helium or air into the airstream. Their results revealed that large-scale eddies tended to break up rapidly in low compressibility, whereas those in high compressibility remained coherent over a longer spatial distance. They also investigated the inclination angle and the size of the large-scale structure, which grows while flowing downstream.

Though these studies contributed to the understanding of the qualitative features of a turbulent large-scale structure, their results were not sufficient for understanding the quantitative features of a mixing mechanism, due to the imprecise aspects of scattering light. Generally, in investigations of high-speed flows, it is very difficult to relate the scattered light intensity from fluid markers directly to a certain physical property. Moreover, when using particles as a fluid marker, a disparity between the particle path and the streamline [1] may result from a lag of the tracing particle [13]. Therefore, many past studies qualitatively regarded light intensity as number density or other properties. On the other hand, using molecular diagnostics, such as acetone PLIF, can provide high-resolution quantitative data and can trace fluid behavior well. Thus, the single-time two-point spatial correlations obtained from acetone PLIF will provide new insight into scalar mixing by the large-scale structure inherent in supersonic mixing flowfields.

The objective of the present work was to examine the geometry and motion of the large-scale structures in the supersonic mixing flowfield created by sonic transverse injection into a Mach 2.0 supersonic mainstream. The single-time two-point spatial correlations of the injectant concentration were obtained from acetone PLIF data. We examined the size, shape, and orientation of those correlations obtained at several locations to clarify the large-scale structure and its motion.

## II. Experimental Apparatus and Data Analysis

### A. Wind Tunnel, Flowfield Conditions, and Acetone PLIF

A suction-type supersonic wind tunnel used in our previous study [14] provided a Mach 2.0 main stream of unheated air in a 200-mm-long test section with a 30 mm square cross section. A sonic air jet was transversely injected from a circular orifice with a 2.5 mm diameter $D$ on a wall of the test section. The flow conditions are summarized in Table 1. The jet-to-mainstream momentum flux ratio $J$ under the isentropic assumption was fixed at $1.87 \pm 0.07$. The Reynolds number based on the mainstream conditions and the duct height was about $3.4 \times 10^5$.

**Table 1 Flowfield conditions**

| Condition | Main | Jet |
|---|---|---|
| Total pressure, kPa | $75.0 \pm 1.2$ | $136.0 \pm 2.5$ |
| Total temperature, K | $291.0 \pm 3.0$ | $291.0 \pm 3.0$ |
| Static pressure, kPa | 11.0 | 71.8 |
| Static temperature, K | 168.2 | 242.5 |
| Flow rate, g/s | 101.1 | 1.72 |
| Mach number | 2.0 | 1.0 |

The flowfield was optically measured with acetone PLIF. The light source was fourth-harmonic radiation from a $Q$-switched pulsed Nd: YAG laser with a wavelength of 266 nm, energy of 70 mJ/pulse, and a maximum repetition rate of 10 Hz. The fluorescence images were recorded using a charge-coupled device camera with a $1024 \times 1024$ array of square pixels. The spatial resolutions were 37.5 $\mu$m/pixel for side-view imaging and 17.5 $\mu$m/pixel for end-view imaging. Gaseous acetone was seeded in only the injectant. The density change of injectant due to acetone seeding was estimated to be 1.4% at the most, and this level of acetone seeding caused a negligible influence on the injectant behavior. Further details of the experiment apparatus, flow conditions, and instrumentation are described in [14].

### B. Uncertainty Analysis

For the PLIF measurement, the overall uncertainty inherent in each fluorescence data point, associated with the elements of error sources tabulated in Table 2, was estimated to be 3.3%. This number translated directly into a relative fluorescence uncertainty of the same amount, which was consistent in magnitude with the degree of repeatability observed for the same fluorescence experiment repeated at different times.

### C. Single-Time Two-point Correlation Analysis Using Acetone PLIF Data

For the present experiment conditions, the fluorescence signal from acetone molecules $S$ is proportional to the acetone molar concentration $C_{\mathrm{acetone}}$ (mol/m$^3$) in the following expressions [1]:

$$S = \mathrm{const} \cdot \frac{\chi_{\mathrm{acetone}} \cdot \rho_{\mathrm{mixture}}}{m_{\mathrm{mixture}}} = \mathrm{const} \cdot C_{\mathrm{acetone}} = \mathrm{const} \cdot \chi_{\mathrm{acetone}_j} \cdot C_j \tag{1}$$

where the seeding rate of the acetone mole fraction in the injectant is constant. Clearly, the LIF signal intensity is proportional to the injectant concentration. Therefore, the spatial correlation of the PLIF signal fluctuations expresses the spatial features of the turbulent scalar field.

The single-time two-point spatial correlation $r(\Delta x, \Delta y)$ was computed by Eq. (2):

$$\begin{gathered} \bar{C}(x, y) = \frac{1}{N} \sum_{i=1}^{N} C_i(x, y), \qquad C'_i(x, y) = C_i(x, y) - \bar{C}(x, y) \\ C'_{\mathrm{rms}}(x, y) = \sqrt{\frac{1}{N} \sum_{i=1}^{N} C_i'^2(x, y)}, \qquad i = 1, 2, \ldots, N \\ r(\Delta x, \Delta y) = \frac{\frac{1}{N} \sum_{i=1}^{N} [C'_i(x, y) \cdot C'_i(x + \Delta x, y + \Delta y)]}{C'_{\mathrm{rms}}(x, y) \cdot C'_{\mathrm{rms}}(x + \Delta x, y + \Delta y)} \end{gathered} \tag{2}$$

**Table 2 Uncertainty estimates in LIF measurement**

| Error Source | Uncertainty, % |
|---|---|
| Shot noise | 1.6 |
| Deviation of acetone seeding | 2.00 |
| Regulated pressure variance | 1.87 |
| Temperature variance | 1.02 |
| **Total uncertainty** | **3.3** |

where point $(x, y)$ is the reference location with which the features are correlated, $C_i(x, y)$ is the instantaneous concentration, $C_i'(x, y)$ is its fluctuation, $\bar{C}(x, y)$ is the average of concentration, $C'_{\mathrm{rms}}(x, y)$ is the standard deviation (STD) of concentration fluctuation, $\Delta x$ is the spatial difference in $x$ direction, and $\Delta y$ is the spatial difference in $y$ direction. In the present study, the highly significantly correlated region with a sample size of 500 was where the absolute value of the correlation coefficient $|r| \geq 0.12$, as determined by statistical testing.

### D. Resolution of PLIF Images

The spatial correlations provide the turbulent mixing information in the pixel-sized basis. Therefore, the key issue for using the statistical analysis is the spatial resolution of the imaging system. In that sense, we checked the relative resolutions defined by the ratio of the probe dimensions and the mass diffusion scale (Batchelor scale), which represents the smallest physical scale at which turbulent mixing is effected by the velocity field. The Batchelor scale $\lambda_B$ is estimated as follows [15–17]:

$$\lambda_B = \delta Re_\delta^{-0.75} Sc^{-0.5} \tag{3}$$

where $\delta$ is the local jet width, $Re_\delta$ is the Reynolds number based on the local jet velocity and width, and $Sc$ is the Schmidt number. A relative resolution is given as $L/\lambda_B$, where $L$ is the largest probe dimension and is equal to the pixel size for the present study. Most of the compressible flow investigation is carried out in a range of 100–700. If $L/\lambda_B < 25$, the measurement can resolve the finest scales [15–17]. For our study, $L/\lambda_B$ is approximately 15, when $\delta = 10$ mm, $Re_\delta = 6.3 \times 10^3$ based on the velocity difference in streamwise direction between the main flow and jet, $Sc = 0.85$, and $L = 37.5$ $\mu$m. This is a relatively better value compared to other studies: 123 with the experiment in normal supersonic injection into a Mach 2.0 supersonic flowfield [15] and 219 with a visualization of hypersonic shear layer using fluorescent tracer species [17]. Therefore, though the spatial correlations in this study is not able to resolve the finest-scale structure because of the relatively larger probe dimension of our imaging system, it has the capability of resolving the large-scale structures.

## III. Results and Discussion

### A. PLIF Visualizations

We examined the time-averaged and single-point turbulent characteristics of the fluctuating concentration field. Figure 1 shows side-view PLIF images: a single-shot image (Fig. 1a), a mean image of 500 frames (Fig. 1b), and a STD image created by 500 frames (Fig. 1c). Figure 1d depicts a mean injectant mole-fraction image quoted from [14]. In images, the average concentration tracks of the maximum, 50%, and 10% are plotted with a dotted line, a solid line, and a dashed-dotted line, respectively. These PLIF images except Fig. 1d were obtained with acetone seeded only in the jet flow so that the contour represents not the mole fraction but the molar concentration (i.e., the number of moles in the specific volume of injectant). The representative instantaneous flow structure of Fig. 1a indicates the existence of the large-scale structures similar to the two-dimensional roller-type vortices produced by low-speed axisymmetric jets. This also indicated the highly intermittent nature of the scalar field on the outer boundary of the jet. But it is not adequate to rely on a single representative image such as Fig. 1a to clarify the existence and behavior of the large-scale structure. Therefore, further investigation should be done to confirm those concerns. We will discuss them in more detail with spatial correlations later. Averaging the single-shot images smeared out the intermittent large-scale structures and resulted in a smoothed well-known injectant plume (Fig. 1b). The standard deviation image of Fig. 1c clearly indicates that the most intensively fluctuating region appeared along the 50% averaged concentration track. This result was reasonable for the intermittent nature of the jet. Therefore, detailed investigation of the 50% track would provide us with many new aspects of the scalar fluctuations in the supersonic turbulent mixing flowfield.

The mean distributions of molar concentration (Fig. 1b) and mole fraction (Fig. 1d) were obviously different especially in the lower part of the jet plume. The molar concentration was a product of local values of acetone mole fraction and density and was affected by changes in either of them; on the other hand, the injectant mole fraction was not affected by the local density and thus represented the true extent of mixing independent of local change of thermodynamic conditions. However, Fig. 2 shows that the maximum, 50%, and 10% tracks of molar concentration and mole fraction were almost the same in the downstream region of $x/D \geq 4$. Figure 3 plots the streamwise decay of the maximum values of mean concentration (dashed line)

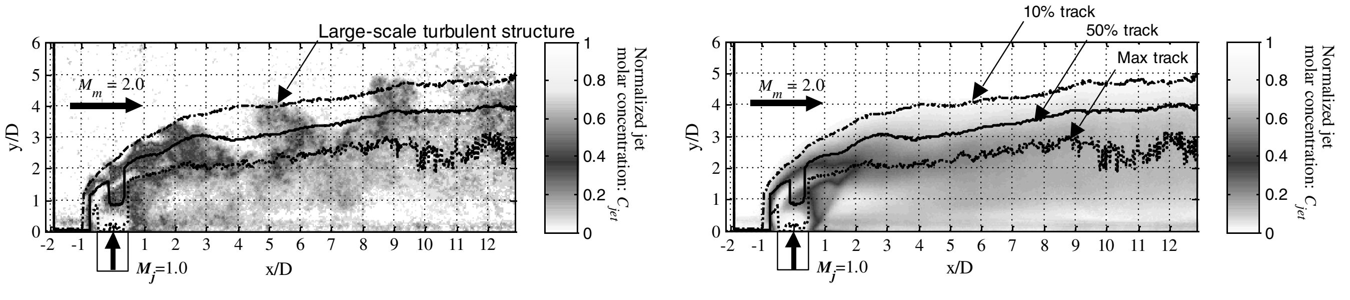

**a) Single-shot image** **b) Averaged image composed of 500 single-shots**

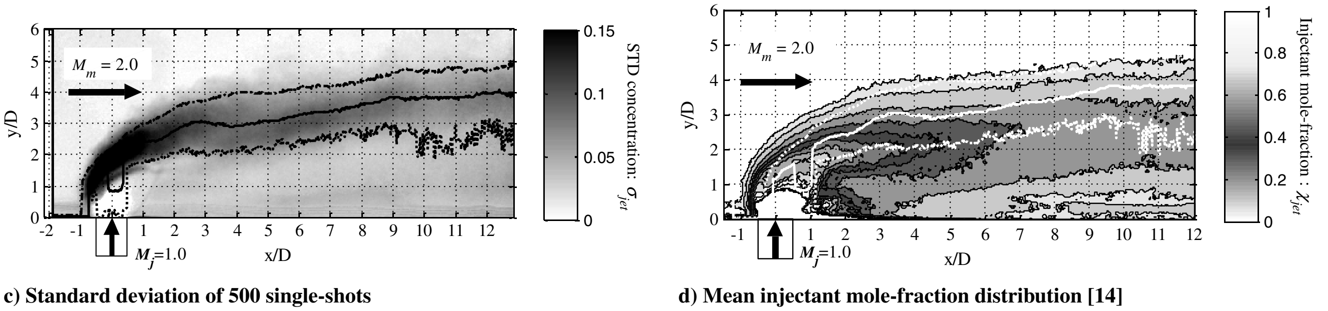

**c) Standard deviation of 500 single-shots** **d) Mean injectant mole-fraction distribution [14]**

**Fig. 1 PLIF images in the center plane. In each image, the average concentration tracks of the maximum, 50%, and 10% are plotted with a dotted line, a solid line, and a dashed-dotted line, respectively.**

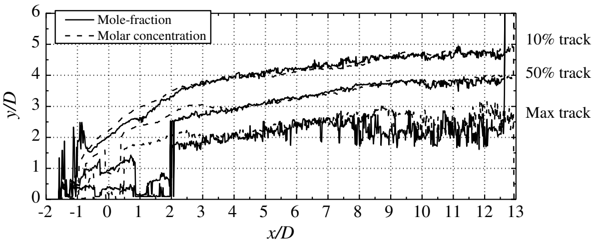

**Fig. 2 Maximum, 50%, and 10% averaged concentration and mole-fraction tracks.**

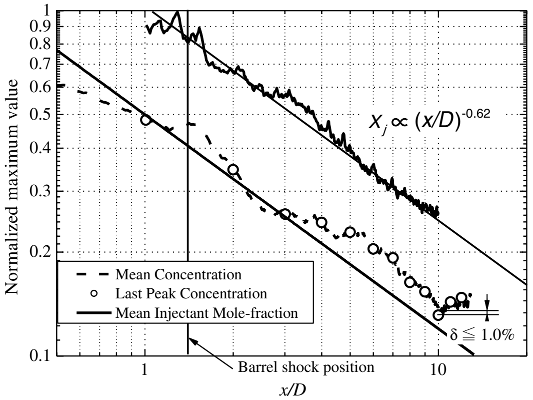

**Fig. 3 Decay of the true maximum and the last peak concentration.**

and mole fraction (solid line). The decay rate of the mean concentration for $x/D \geq 4$ agrees well with that of the mean mole fraction. Therefore, in the downstream region of $x/D \geq 4$, the effect of density change becomes smaller so that the LIF intensity can represent nearly the injectant mole fraction or the injectant mixture fraction.

### B. Self-Similarity in Mean and STD Concentration

We examined the self-similarity of the scalar turbulence field in the outer part of the jet with respect to the mean and standard deviation of concentration. Figure 4a plots the concentration profiles normalized by the maximum concentration in each cross section versus the wall-normal distance normalized by the half-width of the mean concentration profile $(y_{1/2} - y_{\max})$ at each streamwise location. However, since the profile was rather flat near the maximum concentration location for $x/D > 8$ (Fig. 1), the last peak was used instead of the real maximum value for that region. The last peak was defined as the outermost peak in the mean concentration profile and was obtained from the smoothed profile by taking a traveling-average with neighboring 10 pixels for each profile in order to eliminate a noise influence. From Fig. 3, we confirmed that the last peak value of concentration was agreed with the real maximum value within a maximum difference of 1.0%. The normalized mean concentration profiles for the entire region of $0 \leq x/D \leq 12$ (Fig. 4a) agreed fairly well with one another. This result indicates an existence of the self-similarity of the mean concentration in entire region. Figure 4b indicates the standard deviation profiles nondimensionalized by the maximum mean concentration in each cross section versus the same horizontal axis as that used in Fig. 4a. In each profile, the maximum value of fluctuation intensity appeared at $y = y_{1/2}$, where the slope of the mean concentration profile was the steepest and confirms Fig. 1c, for which the most intensively fluctuating region is around the 50% concentration track. For $x/D \leq 5$, the peak value of the nondimensional fluctuation intensity increased as the cross section went downstream, whereas the profiles for the region of $x/D \geq 6$ became quite similar. This result indicated that the outer half of the jet plume took 6*D* to develop so as to have self-similarity of the turbulent property.

### C. Confirmation of Spatial Correlation Analysis

To consider what the correlation coefficient means, we applied the single-time two-point correlation analysis to the main flow without injection. It is almost uniform in the main flow region, except the region having weak shock waves. In the main flow, the concentration fluctuation has almost no meaningful correlation. We can thus confirm that there exists no highly significant meaningful region in the flowfield without injection. The correlated region means that the flow in that region moves together. Results are discussed in detail in [18] and confirmed this expectation. Taking these things into account, we can consider that highly significant correlated regions appearing in the region of interest in this study indicate the turbulent structures.

### D. Spatial Correlation Analysis

We examined the turbulent large-scale structures based on the correlation analysis. Figure 5 presents the two-point correlation maps computed on the entire domain of the side-view LIF image, 400 pixels high by 1000 pixels wide, at intervals of 10 pixels. We have examined how the spacing affects on the resolution of the flow structure. Since a relatively-smaller-scale structure was observed on the periphery of the barrel shock wave, we computed the correlation only in this region. If the spacing is small enough to resolve the smaller scales, then it is enough to resolve the larger-scale structures. Comparison of the spacing was carried out in the region around the barrel shock wave of 100 pixels high by 250 pixels wide,

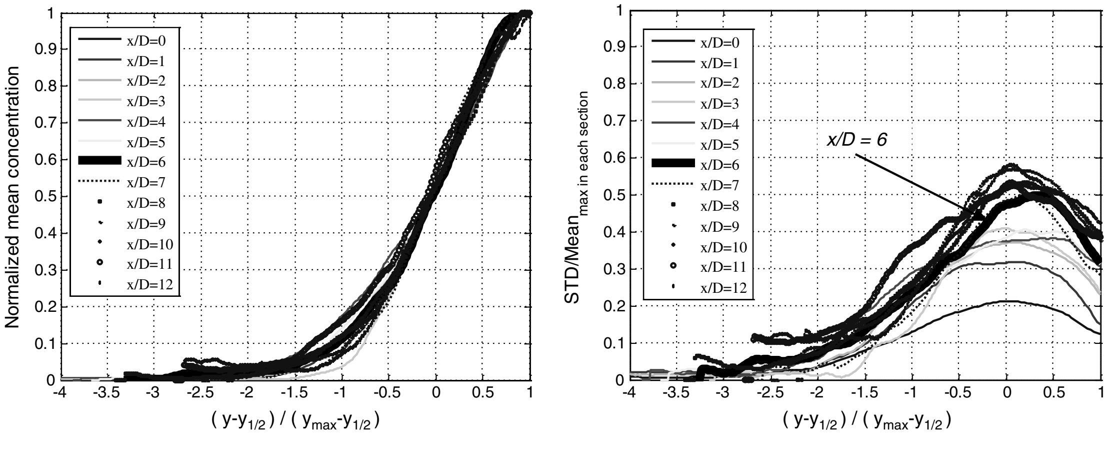

**a) Mean concentration** **b) Fluctuation intensity**

**Fig. 4 Dimensionless profiles of a) mean and b) standard deviation concentration above the maximum concentration track plotted against the wall-normal distance normalized by the half-width of the mean concentration profile, expressed as $(y - y_{1/2})/(y_{\max} - y_{1/2})$ in the streamwise region of $0 \leq x/D \leq 12$.**

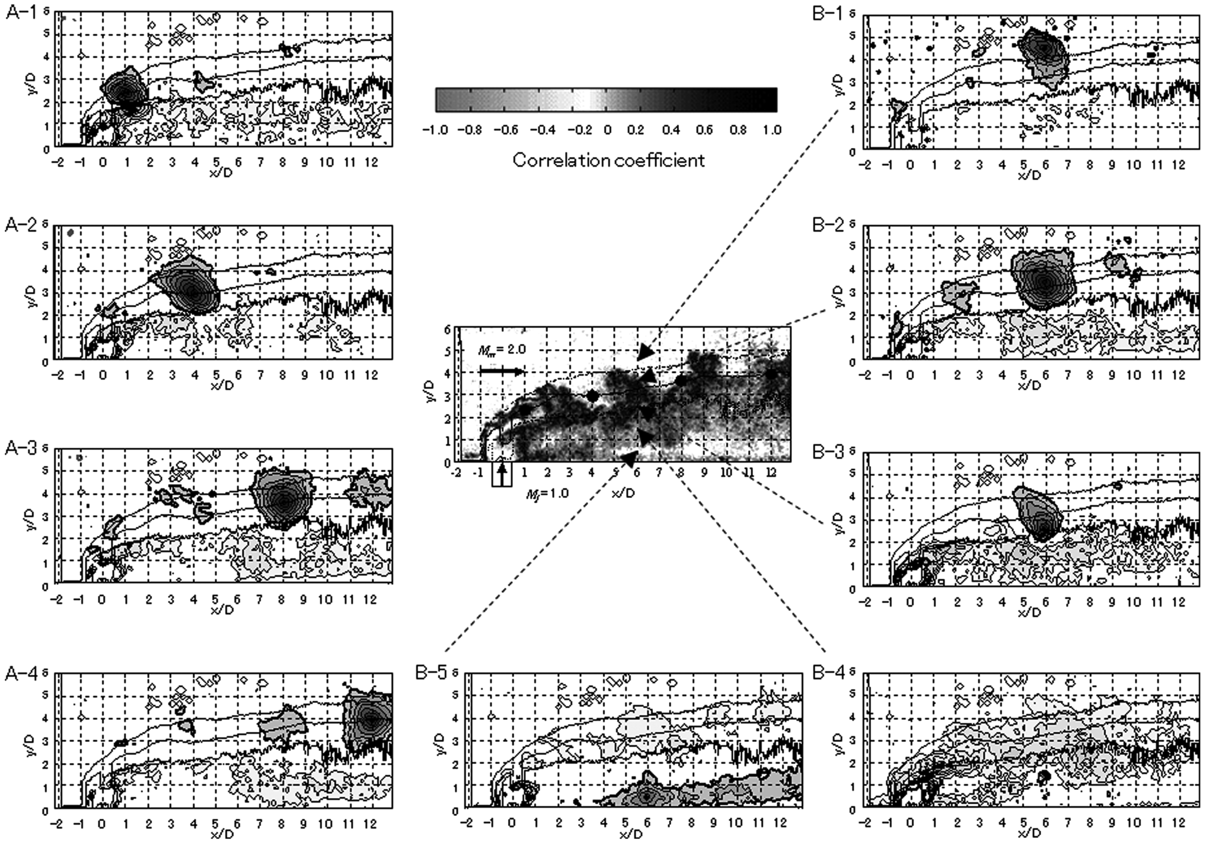

**Fig. 5 Two-point scalar spatial correlation maps in the center plane.**

corresponding to $-2.18 \le x/D \le 1.58$ and $0 \le y/D \le 1.50$. The values of spacing examined were 1, 2, 5, and 10 pixels. Figure 6a presents the averaged PLIF signal intensity, and Fig. 6b presents the computed correlation map. The reference point of correlation is at the black dot in Fig. 6a. Figure 6c presents the correlation profiles on the streamwise line shown in Fig. 6b. Results show that the correlation profiles on a streamwise line for the four spacings exhibit almost no difference, even though they are computed for a relatively-smaller-scale structure. Details are discussed in [18]. Thus, 10 pixels corresponding to $0.15D$ could be considered small enough to

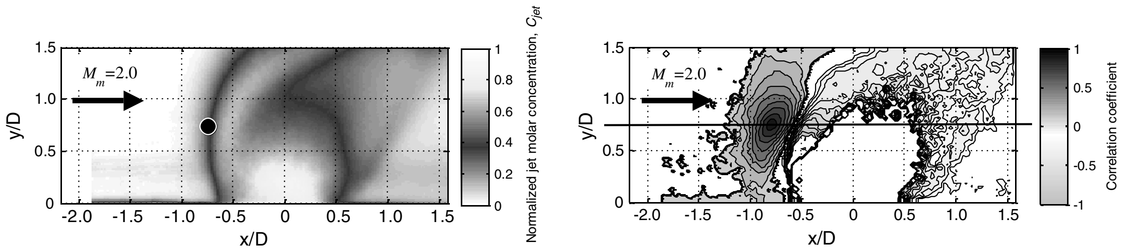

**a) Side-view averaged PLIF image in the barrel-shock region**

**b) Correlation map in the barrel-shock region**

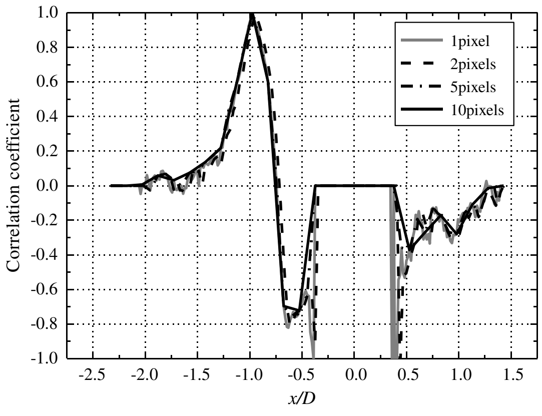

**c) Distributions of correlation coefficient on the line *y/D* = 0.75 in the streamwise direction**

**Fig. 6 Correlation analysis for the barrel shock region in order to examine the spacing effect to resolutions.**

investigate the large-scale features developing in the mid- to downstream regions.

Streamwise change of the correlation is exhibited in Fig. 5, maps A-1 through A-4; the reference locations indicated by black dots were selected on the 50% track of maximum concentration because the concentration fluctuation around this track was the most intensive. Transverse change of the correlation was examined by maps B-1 through B-5; the reference points denoted by arrows were on the line of $x/D = 6$. For all maps, main flow direction is from left to right, and the injection point is $x/D = y/D = 0$. Each correlation map is depicted with the contour levels varying in increments of 0.1 in $0.1 \leq |r| \leq 1.0$. Also, the line of $r = 0.05$ is the outermost contour, and the lines of $r = 0.12$, which indicates the boundary of the highly significantly correlated regions, are highlighted with black.

Streamwise changes of the correlation are exhibited by these maps. The series of correlation maps along the streamwise direction revealed that the high correlation region of each reference position had an inclining elliptic shape and that its geometry changed as it went downstream. Since the correlated region is computed from the fluctuation of concentration, which is a scalar quantity, the shape of correlated region is governed by the flowfield structure. Furthermore, according to Kida [19], an elliptic vortex appears in the shear flow and it rotates depending on the velocity fields. Hence, these results indicate that the large-scale structure, which may stir the jet and main stream, is located around the 50% concentration track. This is consistent with the result of Fig. 1c. Thus, we can confirm that there exists the highly correlation region with some spatial extent that proves the existence of the large-scale structure around the upper jet boundary region. The structure around the maximum concentration track may be small-scale or not very developed, due to remaining high concentration.

To investigate the geometrical development of the large-scale structure in more detail, we made a least-squares curve fit [20] of each high correlation region with an ellipse. Because of above observing results, we focused on the 50% track of the maximum concentration and investigated the size, shape, and orientation of the high correlation regions by putting each reference location on this track. Figure 7 indicates the lengths of major and minor axes of the ellipses and their ratio, and Fig. 8 depicts the inclination angle of the major axis. The error bars denote the minimum and maximum data of the two separate experiment series. Streamwise changes of the sizes of fitted ellipses on the 50% averaged concentration track are plotted. Both the major and minor axes lengths increased as the ellipse moved downstream until $x/D = 6$, then declined gently or maintained a constant level. The ratio of major and minor axes lengths decreased from 1.6 near the injection port to 1.1 at around $x/D = 8$, after which the ratio slightly increased. Figure 8 illustrates changes in inclination angle of the major axis against the streamwise direction. Near the injector port, the major axis of ellipse inclined backward and the absolute value of inclination angle gradually increased until $x/D = 5$, then it turned to decreasing. At around $x/D = 7$, the inclination of the major axis direction switched from backward-leaning to forward-leaning. In this range of $6 \leq x/D \leq 8$, both the ratio of major-to-minor axes and the inclination angle of the major axis changed steeply and simultaneously. These observations revealed that the elliptic large-scale structure first rotated in the clockwise direction as it went downstream until reaching $x/D = 6$, then its shape changed from an ellipse to a circle to another ellipse with switched major and minor axes. Parts of our results were consistent with those of the previous study [12], conducted with a flowfield similar to that used in this study. They reported an increase of inclination angle and a change in shape from elliptic to more circular while moving downstream. They also showed that the level of inclination angle with respect to the streamwise direction ranges from 25 to 45 deg, and they observed the same level of inclination in the mixing-layer investigations [12,21]. Our result in Fig. 8 agrees well, except the axis-switching. The axis-switching of the elliptic structure at $x/D = 7$ was observed in our several experiments conducted separately with similar flow conditions. However, the axis-switching in the present experiment was not so remarkable, because the axis length ratio after the switching was less than 1.3 up to $x/D = 15$. It may be inferred from the entire-flow-seeding PLIF image [14] that the reflected bow shock wave incidents on the jet upper boundary at around $x/D = 16$. As a result of incidence of the reflected shock wave, the turbulent structure was broken up, and hence the correlation region had an almost circle shape, which may correlate to every direction equally. The pairing of the large-scale structures was not clearly observed in the region of observation.

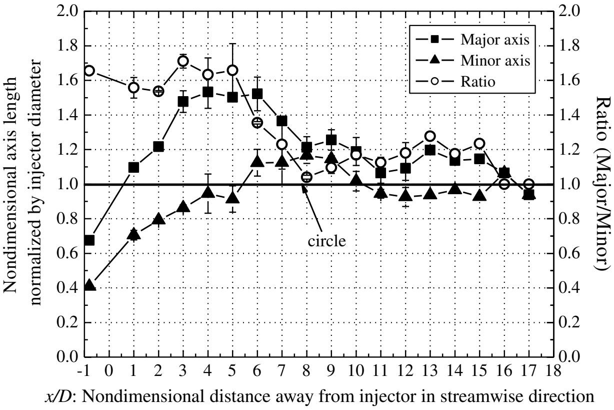

**Fig. 7 Major and minor axes distributions and their ratio (major/minor) along the streamwise direction.**

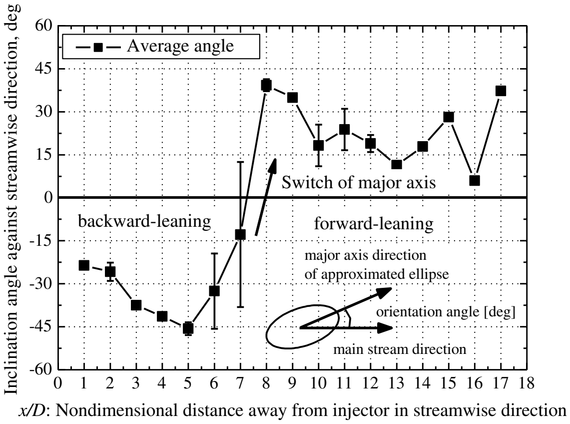

**Fig. 8 Change in inclination angle of fitted ellipse along the streamwise direction.**

Transverse change of the correlation was examined by maps shown in Fig. 5 (B-1 through B-5) on the line of $x/D = 6$. Moving toward the wall from the 50%-of-maximum track, the size of the correlated region evidently became smaller, and the large-scale structure disappeared in the lower part of the jet immediately below the maximum track. The region immediately below the maximum track was always covered with a fully turbulent flow without distinct large-scale structure. The elongated correlated region seen in B-5 near the bottom wall appeared from $x/D = 5$, where the jet completely lifted up from the bottom wall, as seen in the instantaneous PLIF image presented in the center of Fig. 5, and this can be confirmed [14]. This elongated structure might be influenced by the turbulent structure in the boundary layer, because this region was adjacent to the boundary layer. Therefore, this structure might be different from one formed in the upper jet boundary region. This also might result from intermittent inflow of air from outside of the jet plume induced by the counter-rotating vortex pair. It will be discussed in more detail later with the results of the $y$–$z$ plane. In addition to this observation, it is observed for all maps in Fig. 5 that the region above the maximum track was negatively correlated with the region below the maximum track for the entire region. This tendency appearing by turns in either the upper or lower side of the maximum track may suggest that the jet fluids above and below the maximum track move together and result in the flapping or pitching motion. As a result, the correlated regions above and below the

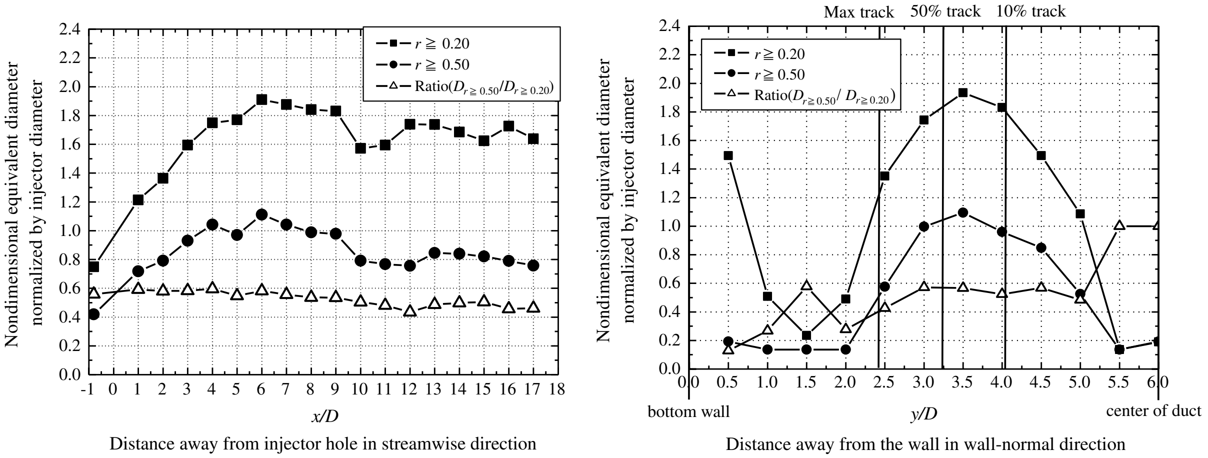

**a) Streamwise distributions on 50% track**

**b) Transverse distributions at $x/D = 6$**

**Fig. 9 Equivalent diameter distribution.**

maximum track have negative correlation. However, this is deduced from only side-view results. Since the jet plume may have highly three-dimensional structure, we need to discuss it further with end-view results. These results indicated that there exist two different types of large-scale structures on the upper and lower boundaries of the injectant plume, and there is no large-scale structure in the central part of the jet.

To quantitatively evaluate the size of the correlated region even when it is not well-fitted with an ellipse, we introduced the equivalent diameter defined by Eq. (4):

$$D_{\mathrm{eq}_{0.2\mathrm{or}0.5}} = 2\sqrt{\frac{A_{r\geq 0.2\mathrm{or}0.5}}{\pi}} \tag{4}$$

where $A_{r\geq 0.2\mathrm{or}0.5}$ denotes the area inside the region, where $r$ is no less than 0.2 or 0.5. Figures 9a and 9b depict the equivalent diameter distributions along the streamwise and wall-normal directions. Each figure plots the equivalent diameters for the regions of $r \geq 0.50$ and $\geq 0.20$ and their ratio. In the streamwise direction, the area inside $r = 0.50$ was about half of that inside $r = 0.20$ and maintained roughly the same level throughout the observed area, whereas the area inside $r = 0.20$ gradually increased. In the transverse direction, both areas changed similarly, taking the maxima between the 10 and 50% tracks. Below the maximum track, their areas sharply decreased to 0.1, which was 8 pixels corresponding to about one-half of a resolution in the present experiment. This result indicates that there was no large-scale structure there.

Next, we consider the reason of changes in the shape and the angle. In general, a fluid element has four motions: transitional motion, rotation, stretch/compression, and shearing deformation. Since the acetone molecules were passively transported in the flowfield, the velocity field strongly influenced the shape and motion of the correlation regions generated by the acetone marker. Ben-Yakar et al. [22] carried out a similar study that employed schlieren photographs with a high-speed camera, and they explained the similar eddy motions as a tilting-stretching-tearing mechanism. Their results showed that the increase of shear and velocity gradients between the main flow and the jet leads to the stretching of the large-scale structures, and the structure tends to tilt toward the fast flow direction. Thus, in order to confirm the mechanism of the rotation and shape change in the present study, we measured the velocity distribution for almost the same flow conditions as this study by a particle image velocimetry system used by Koike et al. [23]. The value of $J$ was $1.8 \pm 0.1$, which was slightly lower than this study.

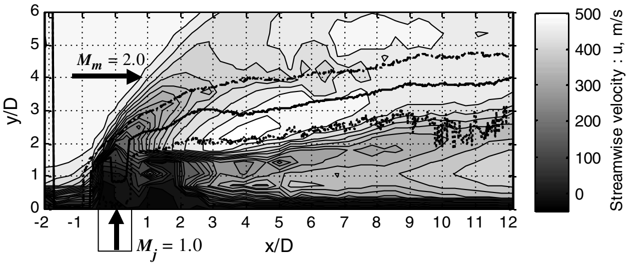

**Fig. 10 Streamwise velocity distribution.**

The streamwise velocity distribution (Fig. 10) confirmed that the velocity in the region between the 10 and 50% tracks was slower than that in the region between the 50% and maximum tracks. Therefore, the part of the large-scale structure inside the 50% track traveled faster than that outside the track; as a result, the structure became backward-leaning. Moving downstream, the streamwise velocity in the outer side of the 50% track gradually became close to that of the inner side. At a distance of $7D$ from the injector, those streamwise velocities became almost the same. In addition, streamwise velocity above the 10% track in this region is faster than that below the 50% track. Thus, these velocity distributions resulted in turning the major axis of the structure normal to the mainstream direction and deforming the elliptic structure to a circular one. To consider the effect of the flapping motion of the jet suggested previously on these results, we also carried out a conditional averaging for correlation analysis. One thousand single-shot images were classified into two groups: one for images for which the concentration at the reference point was under 0.05 and the other for the concentration was over 0.05. The former condition corresponds to the flowfield in which the downstream region on the lower wall was covered with airstream. The reference point of $(x/D, y/D) = (12, 0.09)$ was chosen, because the probability density function distribution created from 1000 single-shot images at this point had a double-peak shape and the saddle point between the two peaks appeared at the value of 0.05. Averaged images, penetration heights, and correlation maps at $x/D = 8$ on the 50% concentration track for both cases were calculated. If the distribution of one group is different from that of the other group, it indicates that the large-scale turbulent structure may be strongly influenced by the motion of the jet, such as flapping. Results showed that there is almost no difference between the two groups and the unconditioned case in the averaged images and correlations. There was only little difference in the maximum tracks and the 50% tracks. The maximum difference between the two groups and the unconditioned case was 6.7%, which was found at the axes ratio of the fitted ellipse of the correlation region. This means that there were no significant flapping motion of the jet in the transverse direction, and the shape change of the correlation region is not mainly caused by jet dynamic motions, but by velocity distributions formed by the local flow structure.

Figure 11 indicates the local convective Mach number, which is defined as the ratio of the speed difference from its maximum in each cross section to the sonic speed at the point of the maximum speed:

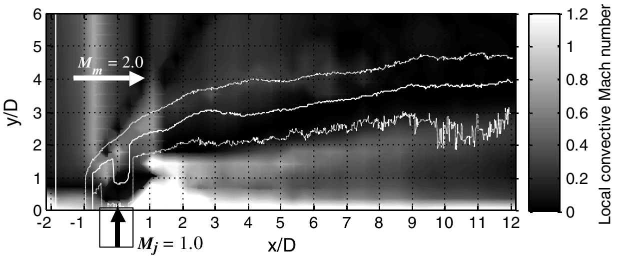

**Fig. 11 Local convective Mach number.**

$$M_{c,\mathrm{local}}|_x = \left.\frac{\upsilon_{\max}-\upsilon_y}{a_{\max}}\right|_x \tag{5}$$

where $M_{c,\mathrm{local}}|_x$ is the local Mach number at the location $(x, y)$, $\upsilon_{\max}$ is the maximum speed in the cross section $x$, $\upsilon_y$ is the local speed at $(x, y)$, and $a_{\max}$ is the acoustic speed at the point at which the maximum speed appears. The speed and the temperature were derived from measured velocity data. Generally, the convective Mach number is defined as the freestream Mach number relative to the moving reference frame of the large-scale structures in the flow; however, in this study, it was defined as indicated above. Though this flowfield was entirely supersonic, the local convective Mach number around the 50% track was very low, obviously less than 0.3 for the entire region. According to Sandham and Reynolds [21], at low $Mc$ (less than 0.4), the two-dimensional Kelvin–Helmholtz instability plays a dominant role in mixing; however, at higher $Mc$ (greater than 0.6), three-dimensional modes are dominant. The large-scale structures similar to those in low-speed jets could thus be formed and exist stably in this flowfield.

The large-scale structure of each reference point was accompanied by several highly correlated regions both upstream and downstream at certain intervals (Fig. 5, maps A-1 to A-4). They corresponded to the adjacent large-scale vortices. Because of the complicated outline of these highly correlated regions, it was difficult to deduce the accurate value of the intervals. However, we qualitatively estimated the interval length in $3D$ to $4D$, or twice of the larger-scale vortex, $D_{\mathrm{eq}_{0.2}}$. These features of the correlation were consistent with the large-scale structure clearly seen in Fig. 1a. However, this large-scale structure was not two-dimensional or axisymmetric, because it was not observed in the lower side of the jet plume. According to previous research, these large-scale vortex structures appearing in intervals may consist of hairpin-vortex structures [3,7,8,22].

Figure 12 presents the end-view PLIF images at $x/D = 4$ with 50 and 10% of the maximum concentration contours: instantaneous image (Fig. 12a), mean image averaged by 300 single shots (Fig. 12b), and mean injectant mole fraction quoted from [14] (Fig. 12c). Though asymmetry was observed in both the instantaneous and the mean concentration images due to density distributions in this plane, the mean injectant mole fraction was distributed symmetrically about the centerline of the cross section. The kidney-shaped distribution in the averaged image indicates the existence of the counter-rotating vortex pair. Similar to the side-view plane, the most intensively fluctuating region is seen in the periphery of the 50% of the maximum concentration track. The same correlation analysis as in the side-view plane was conducted in the end-view planes. For correlation analysis of this end-view image, 300 single-shot images were used; thus, the highly correlated region was $|r| \geq 0.16$. The computed domain was 300 pixels high by 300 pixels wide, corresponding to $0 \leq y/D \leq 4.29$ and $-2.42 \leq z/D \leq 1.86$. The traveling average was taken in the same region as in the side-view plane. The spacing for taking the correlation was 5 pixels, corresponding to $0.07D$. All the contour levels in the end-view correlation maps varied in increments of 0.1 in $0.2 \leq |r| \leq 1.0$, and the line of $r = 0.16$ was added as the outermost contour. In the correlation maps presented in Fig. 13, the reference points were

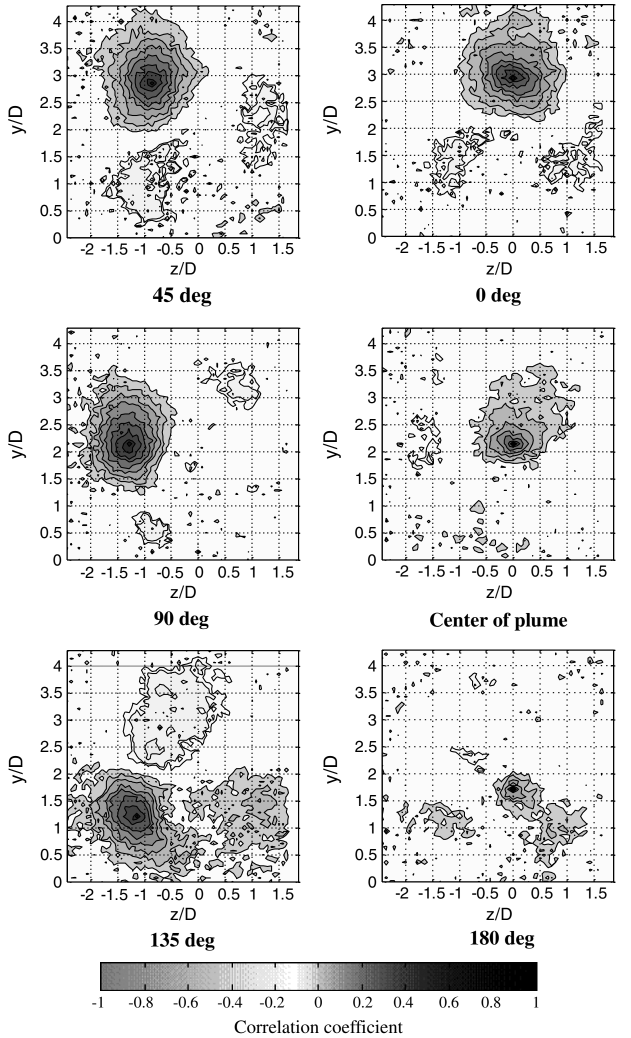

**Fig. 13 End-view spatial correlation map at $x/D = 4$. (The reference points are on the 50% averaged concentration contour and the center of the plume.)**

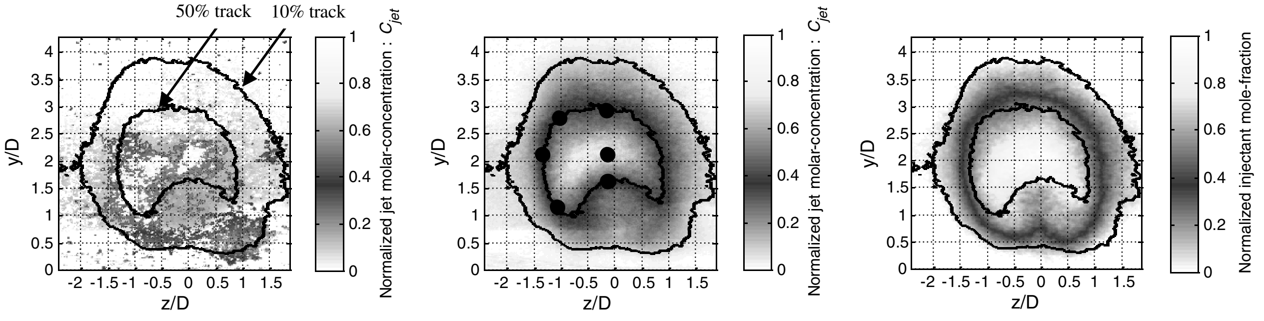

**a) Instantaneous image** **b) Averaged image of 300 shots** **c) Mean injectant mole-fraction**

**Fig. 12 End-view PLIF images at $x/D = 4$ plotted with 50 and 10% of the maximum concentration contours.**

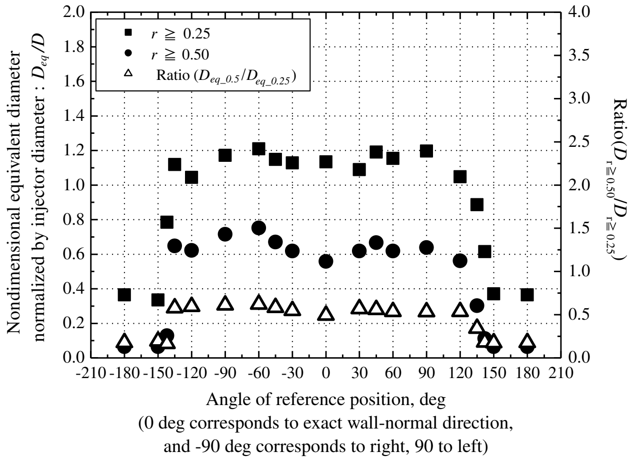

**Fig. 14 Equivalent diameter distribution in $x/D = 4$.**

0, 45, 90, 135, and 180 deg from the centerline of the cross section on the 50% track, and the center of the jet plume was defined as the location at which the concentration profile on the centerline takes the maximum. These maps indicated that the upper central region and both of the lower side regions were negatively correlated. Meanwhile, the right-hand side and the left-hand side in the lower part of the injectant plume were positively correlated. This may correspond to the location of the two counter-rotating streamwise vortices. Slight asymmetry is caused by flapping motion on either the right-hand side or left-hand side due to this counter-rotating motion. In addition, the upper center of the jet plume had little correlation with the lower part of the jet on the centerline. Thus, the jet plume appeared by turns either above or below the side of the center. This result was also consistent with the hairpin-structure model, with the proposed hairpin structure inclined to the jet core [3]. In this figure of 135 deg, the correlated region expands toward the wall. It seems that the air outside and below the jet plume is taken in inside the plume; other laser-based studies support this. Above all, the intensity STD distributions obtained with Mie scattering [12,24,25] showed that significant fluctuations appeared in the region between the two counter-rotating vortices near the bottom wall and probability density function analysis [2] showed that the two vortices act to draw main flow fluid up into the center of the jet. Considering the tendency obtained from this study and those previous studies, the elongated structure in Fig. 5 (map B-5) was generated by intermittent inflow of air from outside of the jet plume induced by the counter-rotating vortex pair.

Figure 14 reveals the circumferential distribution of equivalent diameters inside $r = 0.25$ and 0.50 contours and their ratio on the 50% track in $x/D = 4$. The diameter had local minima at 0 deg and increased as the reference point went to both sides. It remained level from 30 to 90 deg, then decreased to the minimum level from 150 to 180 deg. Figure 15 indicates the nondimensional lengths of the major and minor axes and their ratio of the fitted ellipse. The major axis maintained the same length from 30 to 120 deg on both sides, whereas the minor axis length peaked at 60 to 90 deg: namely, the upper part of the jet plume. From 150 to 180 deg, the sizes of both axes sharply decreased. The ratio of major and minor axes lengths increases as moving downstream, as a whole. As we can see from correlation maps under the jet core in Fig. 13, the correlated regions expanded and they no longer had the elliptic shape. To summarize these trends, the large-scale structure was mostly a circumferentially developed and did not exist in center lower part of the jet.

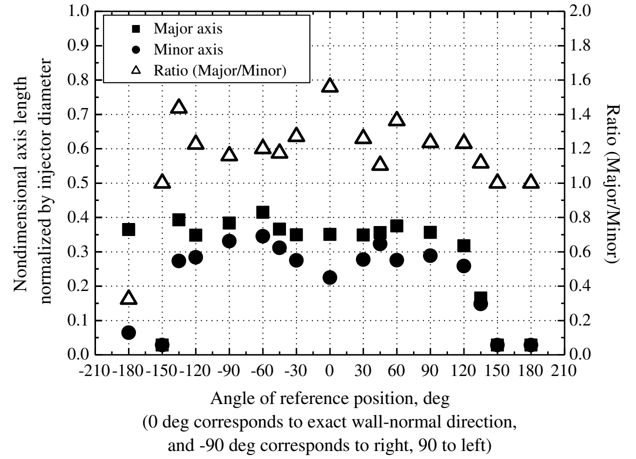

**Fig. 15 Major and minor axes distributions and their ratio (major/minor) in $x/D = 4$.**

## IV. Conclusions

The turbulent structure of the scalar field inherent in the transverse air injection into a Mach 2.0 supersonic airstream was investigated in detail by a single-time two-point spatial correlation analysis based on PLIF data. The following conclusions were drawn for time-averaged characteristics of the scalar turbulence field:

1) Averaged tracks of molar concentration and injectant mole fraction agreed very well with each other in the region of $x/D \geq 4$, though their distributions differed due to local density change.

2) The mean concentration profile in the upper half of the jet plume exhibited self-similarity in the entire region of $0 \leq x/D \leq 12$, whereas the fluctuating intensity took $6D$ to develop itself to have self-similarity.

The following conclusions were drawn for the turbulent large-scale structure analyzed by spatial correlation analysis:

1) A large-scale structure was observed for correlation distributions and appeared along the upper 50% averaged concentration track, where the fluctuation intensity was most intensive. The large-scale structures appeared sequentially in an interval of $3D$ to $4D$, or twice the large-scale vortices; this might consist of the hairpin-vortex-structure models.

2) The size of the large-scale structure grew linearly as it moved downstream until $x/D = 6$, where the fluctuation intensity began to have self-similarity, then shrank gently or maintained a constant size. This tendency is different from that of the mixing layer. In the transverse direction, the area became the maximum between the 10 and 50% averaged concentration tracks and sharply diminished below the maximum track.

3) The structure first had a backward-leaning elliptic shape and rotated itself in a clockwise direction, then its shape changed to a circle and then to a forward-leaning elliptic shape with switching major and minor axes.

4) The streamwise velocity distribution might determine the shape and orientation of the large-scale structure. This suggests that the structure may be controlled by giving such additional velocity distributions as incident shock wave.

5) In the cross sections, the upper center and both lower side regions were negatively correlated, and both the right-hand side and left-hand side of the lower part were positively correlated.

6) The features of the correlation region that appeared alternately in the upper or lower part of the jet plume were ascribed to the intermittent air inflow, which was induced by the counter-rotating vortex pair, at the lower part of the jet from outside of the jet plume.

## Acknowledgments

This work was supported by Research Fellowships of the Japan Society for the Promotion of Science for young Scientists through grant 20086092. The authors express their gratitude to Shuya Shida for his assistance in the experiment.

## References

[1] Takahashi, H., Hirota, M., Oso, H., and Masuya, G., "Measurement of Supersonic Flowfield Using Acetone PLIF," *Transactions of the Japan Society for Aeronautical and Space Sciences*, Vol. 51, No. 174, Feb. 2009, pp. 252–258.
doi:10.2322/tjsass.51.252

[2] VanLerberghe, W. M., Santiago, J. G., Dutton, J. C., and Lucht, R. P., "Mixing of a Sonic Transverse Jet Injected into a Supersonic Flow," *AIAA Journal*, Vol. 38, No. 3, March 2000, pp. 470–479. doi:10.2514/2.984

[3] Lim, T. T., New, T. H., and Luo, S. C., "On the Development of Large-Scale Structures of a Jet Normal to a Crossflow," *Physics of Fluids*, Vol. 13, No. 3, March 2001, pp. 770–775. doi:10.1063/1.1347960

[4] Ganapathisubramani, B., Hutchins, N., Hambleton, W. T., Longmire, E. K., and Marusic, I., "Investigation of Large-scale Coherence in a Turbulent Boundary Layer Using Two-point Correlations," *Journal of Fluid Mechanics*, Vol. 524, Feb. 2005, pp. 57–80. doi:10.1017/S0022112004002277

[5] Ukeiley, L., Tinney, C. E., Mann, R., and Glauser, M., "Spatial Correlations in a Transonic Jet," *AIAA Journal*, Vol. 45, No. 6, June 2007, pp. 1357–1369. doi:10.2514/1.26071

[6] Suzuki, Y., and Kasagi, N., "Turbulent Drag Reduction Mechanism Above a Riblet Surface," *AIAA Journal*, Vol. 32, No. 9, Sept. 1994, pp. 1781–1790. doi:10.2514/3.12174

[7] Zhou, J., Adrian, R. J., Balachandar, S., and Kendall, T. M., "Mechanisms for Generating Coherent Packets of Hairpin Vortices in Channel Flow," *Journal of Fluid Mechanics*, Vol. 387, May 1999, pp. 353–396. doi:10.1017/S002211209900467X

[8] Ganapathisubramani, B., Clements, N. T., and Dolling, D. S., "Large-Scale Motions in a Supersonic Turbulent Boundary Layer," *Journal of Fluid Mechanics*, Vol. 556, June 2006, pp. 271–282. doi:10.1017/S0022112006009244

[9] Messersmith, N. L., and Dutton, J. C., "Characteristic Features of Large Structures in Compressible Mixing Layers," *AIAA Journal*, Vol. 34, No. 9, Sept. 1996, pp. 1814–1821. doi:10.2514/3.13312

[10] Smith, K. M., and Dutton, J. C., "Investigation of Large-Scale Structures in Supersonic Planar Base Flows," *AIAA Journal*, Vol. 34, No. 6, June 1996, pp. 1146–1152. doi:10.2514/3.13205

[11] Miles, R., and Lempert, W., "Two-Dimensional Measurement of Density, Velocity, and Temperature in Turbulent High-Speed Air Flows by UV Rayleigh Scattering," *Applied Physics B, Photophysics and Laser Chemistry*, Vol. 51, No. 1, July 1990, pp. 1–7. doi:10.1007/BF00332317

[12] Gruber, M. R., Nejad, A. S., Chen, T. H., and Dutton, J. C., "Compressibility Effects in Supersonic Transverse Injection Flowfields," *Physics of Fluids*, Vol. 9, No. 5, May 1997, pp. 1448–1461. doi:10.1063/1.869257

[13] Koike, S., Suzuki, K., Kitamura, E., Hirota, M., Takita, K., Masuya, G., and Matsumoto, M., "Measurement of Vortices and Shock Waves Produced by Ramp and Twin Jets," *Journal of Propulsion and Power*, Vol. 22, No. 5, Sept. 2006, pp. 1059–1067. doi:10.2514/1.19330

[14] Takahashi, H., Ikegami, S., Oso, H., Masuya, G., and Hirota, M., "Quantitative Imaging of Injectant Mole Fraction and Density in Supersonic Mixing," *AIAA Journal*, Vol. 46, No. 11, Nov. 2008, pp. 2935–2943. doi:10.2514/1.37783

[15] Murugappan, S., Gutmark, E., Carter, C., Donbar, J., Gruber, M., and Hsu, K.-Y., "Transverse Supersonic Controlled Swirling Jet in a Supersonic Cross Stream," *AIAA Journal*, Vol. 44, No. 2, Feb. 2006, pp. 290–300. doi:10.2514/1.13312

[16] Clements, N. T., and Paul, P. H., "Scalar Measurement in Compressible Axisymmetric Mixing Layers," *Physics of Fluids*, Vol. 7, No. 5, 1995, pp. 1071–1081. doi:10.1063/1.868761

[17] Rossmann, T., Mungal, M. G., Hanson, R. K., "Mixing Efficiency Measurements Using a Modified Cold Chemistry Technique," *Experiments in Fluids*, Vol. 37, 2004, pp. 566–576. doi:10.1007/s00348-004-0851-x

[18] Takahashi, H., "Experimental Study of Scalar Structure in a Supersonic Turbulent Mixing Flowfield Using Acetone PLIF," Ph.D. Dissertation, Aerospace Engineering Dept., Tohoku Univ., Sendai, Japan, March 2009.

[19] Kida, S., "Motion of an Elliptic Vortex in a Uniform Shear Layer," *Journal of the Physical Society of Japan*, Vol. 50, No. 10, Oct. 1981, pp. 3517–3520. doi:10.1143/JPSJ.50.3517

[20] Fitzgibbon, A., Pilu, M., and Fisher, R. B., "Direct Least Squares Fitting of Ellipses," *IEEE Transactions on Pattern Analysis and Machine Intelligence*, Vol. 21, No. 5, May 1999, pp. 476–480. doi:10.1109/34.765658

[21] Sandham, N. L., and Reynolds, W. C., "Compressible Mixing Layer: Liner Theory and Direct Simulation," *AIAA Journal*, Vol. 28, No. 4, 1990, pp. 618–624. doi:10.2514/3.10437

[22] Ben-Yakar, A., Mungal, M. G., and Hanson, R. K., "Time Evolution and Mixing Characteristics of Hydrogen and Ethylene Transverse Jets in Supersonic Crossflows," *Physics of Fluids*, Vol. 18, 2006, p. 026101. doi:10.1063/1.2139684

[23] Koike, S., Takahashi, H., Tanaka, K., Hirota, M., Takita, K., and Masuya, G., "Correction Method for Particle Velocimetry Data Based on the Stokes Law," *AIAA Journal*, Vol. 45, No. 11, Nov. 2007, pp. 2770–2777. doi:10.2514/1.30962

[24] Gruber, M. R., Nejad, A. S., Chen, T. H., and Dutton, J. C., "Mixing and Penetration Studies of Sonic Jets in a Mach 2 Freestream," *Journal of Propulsion and Power*, Vol. 11, No. 2, March 1995, pp. 315–323. doi:10.2514/3.51427

[25] Gruber, M. R., Nejad, A. S., Chen, T. H., and Dutton, J. C., "Transverse Injection from Circular and Elliptic Nozzles into a Supersonic Crossflow," *Journal of Propulsion and Power*, Vol. 16, No. 3, May 2000, pp. 449–457. doi:10.2514/2.5609

E. Gutmark
*Associate Editor*